Composites: Part A 103 (2017) 25–34

Contents lists available at ScienceDirect

Composites: Part A

journal homepage: www.elsevier.com/locate/compositesa

Magnetoactive elastomer/PVDF composite film based magnetically controllable actuator with real-time deformation feedback property

Jiabin Feng [a], Shouhu Xuan [a,b,*], Li Ding [a], Xinglong Gong [a,*]

[a] CAS Key Laboratory of Mechanical Behavior and Design of Materials, Department of Modern Mechanics, University of Science and Technology of China, Hefei 230027, People's Republic of China

[b] National Synchrotron Radiation Laboratory, University of Science and Technology of China, Hefei 230027, People's Republic of China

ARTICLE INFO

Article history:
Received 31 May 2017
Received in revised form 4 September 2017
Accepted 5 September 2017
Available online 8 September 2017

Keywords:
A. Polymer-matrix composites (PMCs)
A. Smart materials
B. Magnetic properties
B. Mechanical properties
Magnetoactive elastomer

ABSTRACT

This work reported a high performance flexible magnetically controllable actuator based on magnetoactive elastomer (MAE) and poly (vinylidene fluoride) (PVDF) composite film. The magnetic-mechanic-electric coupling properties of the actuator were systematically investigated by cyclical wrinkle, magnetic bending, and stretching test. The induced charge under a magnetic bending can reach as large as 158 pC even at small magnetic field of 100 mT with the bending angle up to almost 90° within 0.6 s. Moreover, a new model was proposed to theoretically reveal the intrinsic correspondence. The model matches well with the experimental results. Based on this kind of actuator, a magnetically controllable tentacle is developed, which could grasp, transport, and release object by switching the supplied current. Due to the real-time deformation feedback characteristics, this kind of actuators can find wide applications in actively controllable engineering, artificial robotics, and biomedicine.

1. Introduction

Intelligent soft active materials are of enticing prospect for the realization of specific functionalities beyond traditional materials [1]. Diverse types of stimulation principles, including electric fields [2], heat [3], chemicals [4], and magnetic fields [5], have been extensively explored for the potential applications. The mechanic and electric properties of the intelligent soft active materials, such as materials shape, stiffness, and resistance, can be altered by external stimulations [6]. Such active materials have been widely employed in various highly functional devices such as micropumps [7], sensors [8], inductors [9], actuators [10], and some other microfluidic [11] or bioengineering [12] systems. All the actuation methods have their own outstanding advantages for the realization of active control in different conditions. Among diverse stimulation principles, the magnetic actuation results in a particularly enticing alternative for controlling the intelligent devices in a direct and simple way with long distance controllability and fast response ability [13].

Magnetoactive elastomer (MAE) is a new class of smart materials with magnetic particles, such as carbonyl iron particles, dispersed in soft elastomer matrix [14]. This kind of materials is an ideal candidate for magnetic manipulation [15]. The embedding magnetic particles in soft elastomer can be arranged to form desired chain-like structures during the vulcanization process [16,17]. The mechanical properties of MAE, such as stiffness and damping, can be reversibly altered by the external magnetic field [18]. Thus, the MAE has a wide range of applications relating to tunable vibration absorbers [18], isolators [19], inductors [9], sensors [20], pumping devices [7], etc. Unfortunately, the traditional MAE is unsuitable for actuators due to the poor flexibility. To improve the performance of MAE in specific environments especially required high flexibility, a new thin film of MAE with high magnetic sensitivity, low stiffness, and high flexibility has been developed. The high saturated magnetization of magnetic particles endows the MAE film with an exceptional functionality for quick response to the external magnetic field [21,22]. The low stiffness of MAE film enables the capability of intense deformation under small force induced by magnetic field [23]. Therefore, the MAE film is particularly enticing for creating multifunctional actuators in complex environments [24,25]. In previous studies, an anisotropic elastomer film with chains of magnetic nanoparticles aligned in selected directions was fabricated [17]. The selective and directional actuation was eventually realized under uniform magnetic fields or field gradients. Alternatively, a flowerlike soft platform driven by magnetic field was prepared by three-dimensional laser

* Corresponding authors at: CAS Key Laboratory of Mechanical Behavior and Design of Materials, Department of Modern Mechanics, University of Science and Technology of China, Hefei 230027, People's Republic of China.

E-mail addresses: xuansh@ustc.edu.cn (S. Xuan), gongxl@ustc.edu.cn (X. Gong).

http://dx.doi.org/10.1016/j.compositesa.2017.09.004
1359-835X/

printing [26]. The platform can grasp and transport a cargo to targeted area in the air and a variety of liquids.

However, in previous works, the deformation of the actuators remains unknown in actuation process [17,26]. The deformation is very important for information feedback and further active control. Thus, the *in situ* detection of the deformation is required for intelligent magnetically controllable actuators. Fortunately, poly (vinylidene fluoride) (PVDF) happens to be an exceptional component to realize the real-time measurement of deformations due to its excellent piezoelectricity and flexoelectricity [27–29]. A large number of charges are generated on the surface of PVDF when suffering from stretching, compressing, and bending deformation. The induced charge can be used to evaluate the relevant force and deformation [30]. Recently, a particular high flexoelectric coefficient of the order 10^{-8} C/m in PVDF polymer was reported with excellent linearity between electric current and deflection [31]. Moreover, the ultrathin PVDF film exhibits high mechanical strength, excellent flexibility, and good stability, which are very important for the final practical applications. Therefore, the PVDF is a perfect supplement to MAE film for the realization of deformation measurement and active control. The combination of MAE and PVDF film shows promising prospects in artificial robotics and intelligent control. To our knowledge, the MAE/PVDF hybrid actuator with both magnetic actuation and real-time deformation detecting has not been reported.

Herein, a high performance magnetically sensitive, controllable, and flexible actuator with the combination of MAE and PVDF film was fabricated by using spin coating and tape casting technologies. The magnetic-mechanic-electric coupling properties were systematically studied by cyclical wrinkle, magnetic bending, and magnetic stretching experiments. The pure bending effect could be calculated by subtracting the magnetic stretching effect from the magnetic bending result. A nearly linear relationship between induced charge and bending angle was experimentally presented. A novel model was proposed to study the substantial bending angle dependency of induced charge. Moreover, an enticing magnetically controllable tentacle was subsequently fabricated. The tentacle can grasp, transport, and release the ABS plastic in air. Meanwhile, the deformation of the tentacle can be real-time measured. This class of magnetically controllable and flexible actuators has promising prospect for realizing artificial intelligent actuation in complex environments.

2. Experimental

2.1. Materials

The polydimethylsiloxane (PDMS) precursor and curing agent (Sylgard 184) were obtained from Dow Corning. According to the specification from Dow corning, the average numeral molecular weight of PDMS (10:1 ratio) is 27,000. The PDMS was used as the matrix of magnetoactive elastomer (MAE) and packaging material in actuator fabrication process. The carbonyl iron (CI) particles provided by BASF in Germany was used as the magnetic filler in MAE. The average size of CI particles is 7 μm. The Poly (vinylidene fluoride) (PVDF) pellets (average $M_w = 530,000$) were purchased from Sigma-Aldrich. The N-methyl pyrrolidone (NMP) used as the solvent of PVDF was provided by Aladdin chemical Co., Ltd.

2.2. Fabrication of MAE/PVDF based multilayer actuator

Pure PDMS mixture was prepared by mixing 5 g PDMS precursor and 0.5 g curing agent together. The mixture was sufficiently blended by stirring for 10 min and sonicating for 10 min. Then, the mixture was degassed in a vacuum container under 0.2 bar absolute pressure for 20 min to remove the trapped bubbles. The PDMS film was obtained by pouring the final mixture onto a silicon wafer, spin-coated at 1000 rpm for 60 s and cured at 100 °C for 10 min. The PDMS film was remained on the surface of silicon wafer for the following preparation (Fig. 1). Subsequently, 5.5 g CI particles and 0.5 g PDMS curing agent were added into 5 g PDMS precursor. The mixture was stirred using mechanical stirring and sonicated for 10 min, respectively. Then, the trapped bubbles were removed by degassing the mixture in a vacuum container under 0.2 bar absolute pressure for 20 min. After that, the mixture was poured on the surface of above PDMS film. Then, the MAE mixture was spin coated at 1000 rpm for 60 s and cured at 100 °C for 10 min. Then, the MAE-PDMS bilayer was obtained with strong combination between MAE and PDMS film. The resulting MAE-PDMS bilayer film was released from the silicon wafer by manual peeling (Fig. 1).

The PVDF solution was prepared by dissolving 6 g PVDF pellets in 60 mL NMP at 60 °C for 2 h. The solution was degassed in a vacuum container under 0.2 bar absolute pressure for 20 min to remove the trapped bubbles. Then, the solution was poured onto a clean, smooth, and horizontal glass plate fixed at the centre of the oven. Finally, the solution was evaporated at 90 °C for 12 h and annealed at 120 °C for 8 h to obtain the PVDF film. Then, the PVDF film was overgilded on both sides by using magnetron sputtering. Two wires were connected to each gold electrode of PVDF film by using conductive adhesives. Then, the PVDF film was placed on the top surface of MAE-PDMS bilayer close to the PDMS. A thin PDMS liquid layer was brushed on the surface of PVDF film to package the PVDF film and MAE-PDMS bilayer together. After curing at 60 °C for 48 h, the multilayer was obtained. The actuator was obtained by cutting the multilayer into a specific shape (Fig. 1).

2.3. Characterization

The microstructure of the multilayer was observed by using a scanning electron microscope (Philips, Model XL-30 ESEM-FEG, The Netherlands). The accelerating voltage was 20 kV. The hysteresis loop of CI particle and MAE film were tested by HyMDC (Hysteresis Measurement of Soft and Hard Magnetic Materials). X-ray diffraction (XRD) and Fourier Transform infrared spectroscopy (FTIR) were used to characterize the content of MAE and the phase structure of PVDF (Fig. S1).

2.4. The magnetic-mechanic-electric coupling properties analysis

The Young's modulus of MAE, PVDF, and multilayer was investigated under uniaxial stretching by using Material Testing Systems (MTS) (MTS criterion 43, MTS System Co., America) (Fig. S2). A custom measurement system consisted of charge amplifier (DH5863, DONGHUA Corp., China) (set value: 3.00 pC/unit, 30 mV/unit) and dynamic signal analyzer (SignalCalc ACE, Data Physics Corp., America) was designed to measure the charge induced by the deformation of actuator (Fig. S3). The magnetic-mechanic-electric coupling properties of actuator were investigated by instron Universal Testing Systems (E3000K8953, Instron System Co., America) and a self-designed cantilever beam measurement system. The external magnetic field was generated by a large electromagnet.

3. Results and discussion

3.1. Characterization of MAE, PVDF, and multilayer film

SEM micrographs of the MAE, PDMS, PVDF, and multilayer film are shown in Fig. 2. The CI particles are spread randomly in PDMS

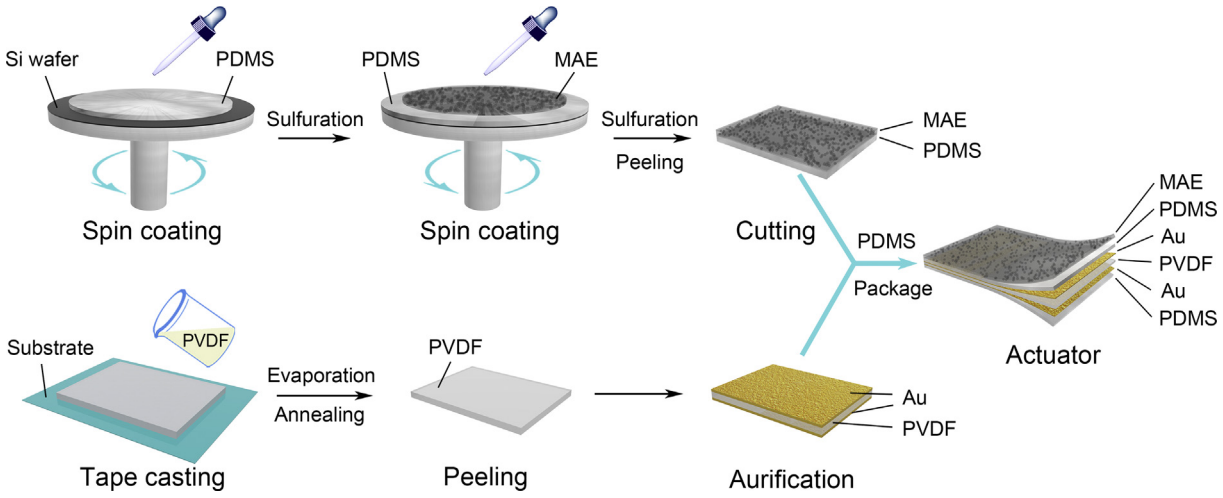

Fig. 1. Schematic illustrations of actuator preparation. (For interpretation of the references to color in this figure legend, the reader is referred to the web version of this article.)

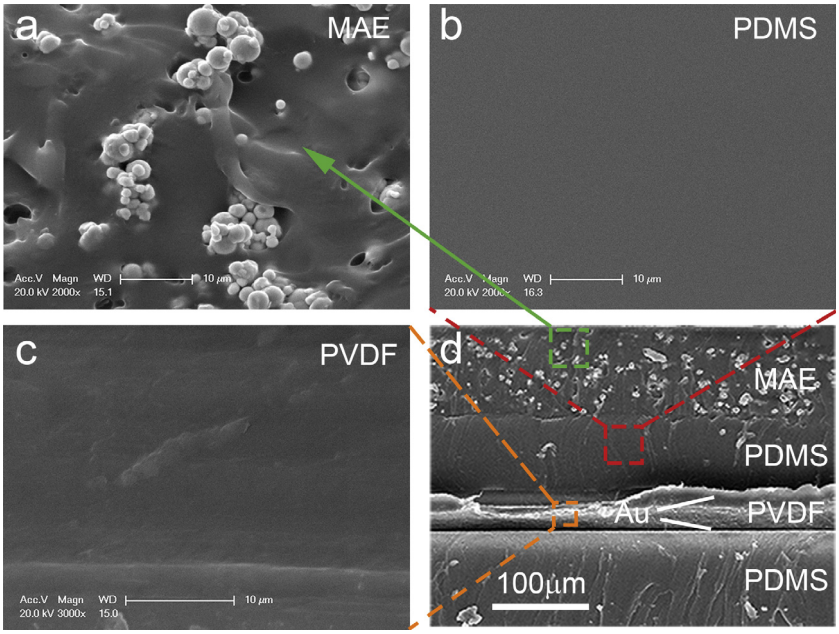

Fig. 2. SEM image of (a) MAE film, (b) PDMS film, (c) PVDF film, and (d) multilayer film. (For interpretation of the references to color in this figure legend, the reader is referred to the web version of this article.)

matrix with strong combination to the PDMS base polymer (Fig. 2a). The PDMS and PVDF film are neat and homogeneous (Fig. 2b and c). The order of the films in multilayer film is MAE/PDMS/Au/PVDF/Au/PDMS (Fig. 2d). The Au film is difficult to identify due to the ultrathin thickness of 100 nm. The average thickness of MAE, PDMS, and PVDF film are nearly 80 μm, 80 μm, and 30 μm, respectively. No air or crack is found between two nearby layers and the combination shows high bond strength. The hysteresis loop of CI particles and MAE film are shown in Fig. 3a. The CI particles and MAE film could be saturated at a small magnetic field strength of 300 kA/m. The saturation magnetization of CI particles and MAE film are 236 emu/g and 118 emu/g, respectively. The magnetization curve is essentially coincident with the demagnetization one. No magnetic hysteresis and remanence are presented. Thus, the MAE film is a soft magnetic material and sensitive to magnetic field. The FTIR spectrum of PDMS and MAE shows that the MAE film contains PDMS (Fig. 3b). As a semicrystalline polymer, α-phase, β-phase, and γ-phase exist in PVDF [32]. The FTIR and XRD technology were applied to study the crystal structure of pure PVDF film. The FTIR spectrum of pure PVDF film is shown in Fig. 3c. The strong absorption peak at 763 cm^{-1} is assigned to the characteristic peaks of the α-phase. Peak at 840 cm^{-1} is the common characteristic of β-phase [33]. Meanwhile, the crystallinity of the pure PVDF film is evaluated by XRD (Fig. 3d) [34]. The peaks at $2\theta = 17.6°$ (1 0 0) and 18.6° (2 0 2) correspond to α-phase, while the peak at $2\theta = 20.6°$ (1 1 0) is the characteristic β-phase for PVDF. The FTIR spectrum and XRD pattern results demonstrate that the α-phase and β-phase coexist in the PVDF film. The relative fractions of α-phase and β-phase are 44.5% and 55.5%, respectively.

Then, the Young's moduli of MAE, PVDF, and multilayer film were studied by MTS (Fig. 4a). For 50 wt% MAE film, the tensile stress is linear with the applied strain. The MAE film exhibits elasticity before the failure at strain of 48% (Fig. 4b). In small strain level, the tensile

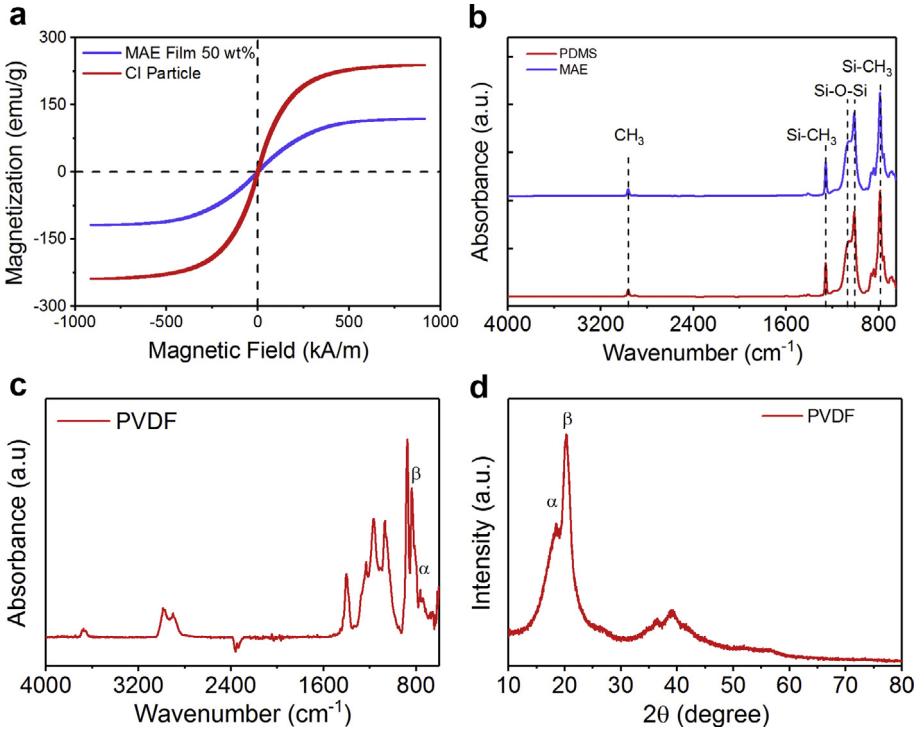

Fig. 3. (a) Hysteresis loop of carbon iron particles and 50 wt% MAE film. (b) FTIR spectra of PDMS and MAE film. (c) FTIR spectrum of pure PVDF film. (d) XRD pattern of pure PVDF film. (For interpretation of the references to color in this figure legend, the reader is referred to the web version of this article.)

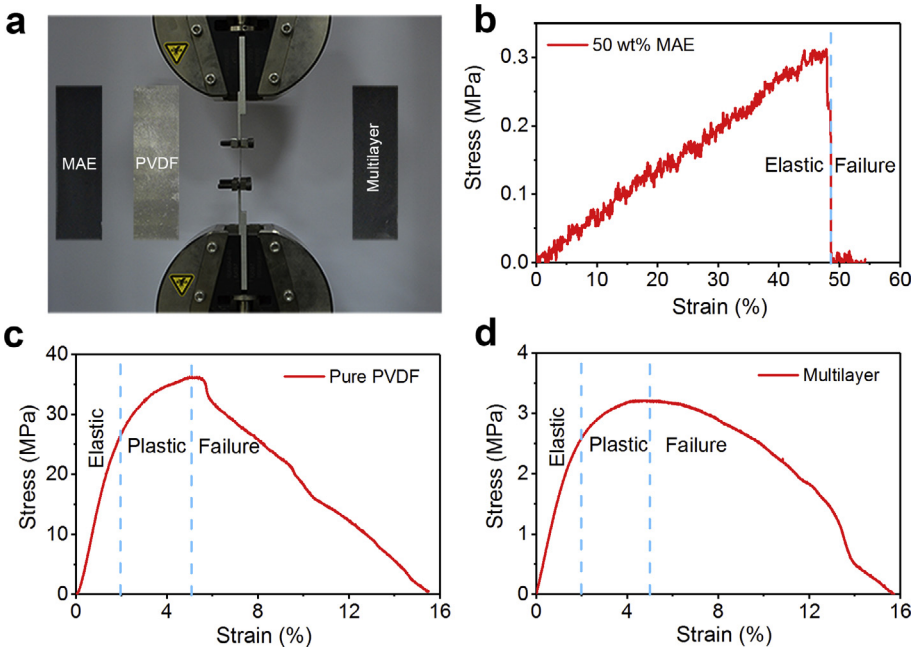

Fig. 4. (a) Experimental setup of uniaxial tensile measurements using MTS. Stress-strain curves of (b) 50 wt% MAE film, (c) pure PVDF film, and (d) multilayer. (For interpretation of the references to color in this figure legend, the reader is referred to the web version of this article.)

stress of pure PVDF and multilayer are nearly linear when the applied strain is within 2%. Then, the samples go through a plastic state before finally failure appeared at nearly 5% strain (Fig. 4c and 4 d). The maximum tensile strength of MAE, PVDF, and multilayer film within elastic range are 0.30 MPa, 26.9 MPa, and 2.61 MPa, respectively. The elastic strain of MAE film can reach as large as 48%, while the elastic strain of PVDF and multilayer film are nearly 2%. Thus, the calculated Young's moduli of MAE, PVDF, and multilayer film are 0.63 MPa, 1.35 GPa, and 130 MPa, respectively. The experimental results demonstrate that the PVDF enhances the stiffness of multilayer compared with MAE, and the resulting multilayer shows high mechanic strength.

3.2. The magnetic-mechanic-electric coupling properties of actuator

As MAE film can be forced to move, the PVDF film will follow the deformation of the MAE film to stretch or bend. The PVDF is an excellent piezoelectric and flexoelectric material (Fig.5a) [31]. When stretching the PVDF, the distance between two nearby CH_2 or CF_2 dipoles will be enlarged. Then, the change of dipoles will induce positive and negative charges on the two sides of PVDF film, respectively (Fig.5b). When bending the PVDF, the distance between dipoles along the outer surface will increase, while the dipoles along the inner surface will be closer (Fig.5c). In this case, the negative charges will be produced on the outer surface and the positive charges will be induced on the inner surface. Meanwhile, the induced positive and negative charges have the equal magnitude. Moreover, the characterization of induced charge on one side of PVDF is sufficient to investigate the properties of PVDF. Thus, only one channel of induced charge is presented in the following tests.

3.2.1. The cyclic wrinkle experiment

For further study, we fabricated an actuator by using the multilayer film. The length and width of the actuator are 40 mm and 20 mm, while the length and width of PVDF film within the actuator are 36 mm and 17 mm. A cyclic wrinkle experiment was firstly carried out to investigate the mechanic-electric properties of the actuator using instron (Fig. 6a). The actuator was straight at the initial condition with the gap between two chucks set as 22 mm. Then, the actuator was forced to wrinkle coincide with the displacement of instron chuck. A triangular wave was chosen as the input control stimulus. The displacement was set as 2 mm, 4 mm, 6 mm, and 8 mm, and the velocity was 500 mm/min, 1000 mm/min, 1500 mm/min, 2000 mm/min, and 2500 mm/min. At 2 mm and 500 mm/min, the induced charge roughly changes from −19.6 pC to 19.8 pC and the peak-to-peak (P-P) charge is 39.4 pC (Fig. 6b). No hysteresis is found between displacement and induced charge, which means that the actuator can quickly response to imposed displacement. To study the displacement-dependent properties, the velocity was fixed at 500 mm/min and the displacement varied from 2 mm to 8 mm (Fig. 6c). The induced P-P charge increases with displacement due to the high deformation sensitivity (Fig. 6c). The velocity-dependent properties were also investigated with the variation of velocity from 500 mm/min to 2500 mm/min at the displacement of 8 mm. The induced P-P charges at different velocities are almost the same (Fig. 6d). Thus, the actuator is insensitive to motivating velocities. The repeatability property of the actuator was investigated by cyclic wrinkle experiment using MTS (Fig. 7). The input signal was set as triangular wave. The cycle frequency and displacement were 1 Hz and 2 mm, respectively. The repeatability of the actuator is excellent after 1000 cycles. The result indicates that this kind of actuator can be used in practical applications.

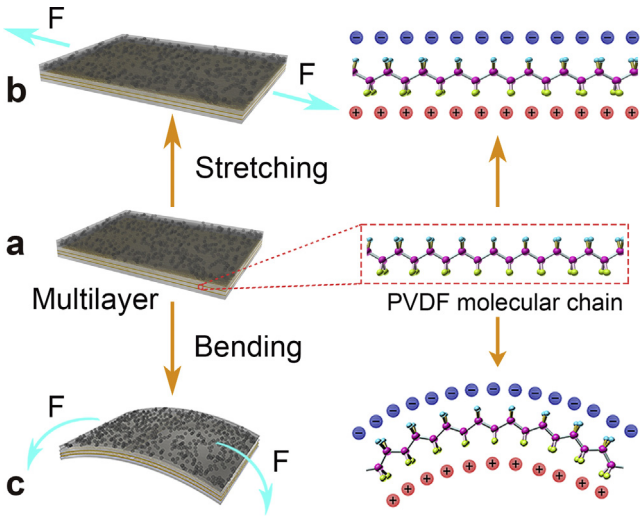

Fig. 5. (a) Schematic illustration of the actuator and PVDF molecular chain. Schematic illustration of the (b) stretched and (c) bent actuator as well as the induced charge along the PVDF molecular chain. (For interpretation of the references to color in this figure legend, the reader is referred to the web version of this article.)

3.2.2. The magnetic bending experiment

As a new kind of smart magnetically controllable material, the magnetic response properties play a critical role in practical applications. Thus, the magnetic response properties of the actuator need to be systematically explored. Herein, a magnetic bending experiment was firstly carried out to investigate the magnetic-mechanic-electric coupling properties of the actuator. The actuator was fixed in a gap between two large electromagnets. The current of the two electromagnets remained off at initial state. The actuator nearly kept in a horizontal state perpendicular to the magnetic field. When turning on the current and imposing a given magnetic field, the actuator bent rapidly to almost 90° (Fig. 8a). After switching off the current, the actuator sprang back to initial state. The bending induced charge at 100 mT, 200 mT, 300 mT, and 400 mT are 167 pC, 175 pC, 184 pC, and 196 pC, respectively (Fig. 8b). The bending induced charge meets an increment with magnetic field. Under different magnetic fields, the bending time is nearly the same value of 0.55 s (Fig. 8c). The bending induced current could be calculated by dividing the charge by time. The bending induced current increases with magnetic field (Fig. 8d).

3.2.3. The magnetic stretching experiment

As discussed above, the external magnetic field can bend and stretch the actuator. Magnetic bending and stretching effect are both existed in magnetic bending experiment. Moreover, the magnetically induced force is very important for practical applications and should be accurately measured. To obtain the pure bending response properties of the actuator, a magnetic stretching experiment was carried out to eliminate the magnetic stretching effect from magnetic bending experiment. Meanwhile, a custom cantilever beam was employed to measure the stretching force of the actuator at external magnetic field in magnetic stretching experiment (Figs. 9a and S4). The length, width, and depth of the cantilever beam are 63 mm, 30 mm, and 0.8 mm, respectively. The actuator was fixed at the end of the cantilever beam perpendicular to it. The actuator, as well as cantilever beam, was placed in the gap between two electromagnets. The actuator was parallel to the magnetic field. The stretching induced charge at 100 mT, 200 mT, 300 mT, and 400 mT are 8.54 pC, 17.7 pC, 26.2 pC, and 34.6 pC, respectively (Fig. 9b). The stretching induced charge is nearly linear with the magnetic field, but the stretching induced charge is far less than bending results. Meanwhile, the stretching time almost keeps constant for different magnetic field (Fig. 9c). The stretching time is nearly the same as bending time. An increment is also found between the stretching induced current and magnetic field (Fig. 9d). Furthermore, the deflections of the cantilever beam at different magnetic fields were measured by digital image processing. The deflection significantly increases with magnetic field, which implies a positive correlation between the magnetically induced force and magnetic field.

3.2.4. The weighting experiment

In order to acquire the magnetically induced force, a weighting experiment was set up to measure the bending stiffness of can-

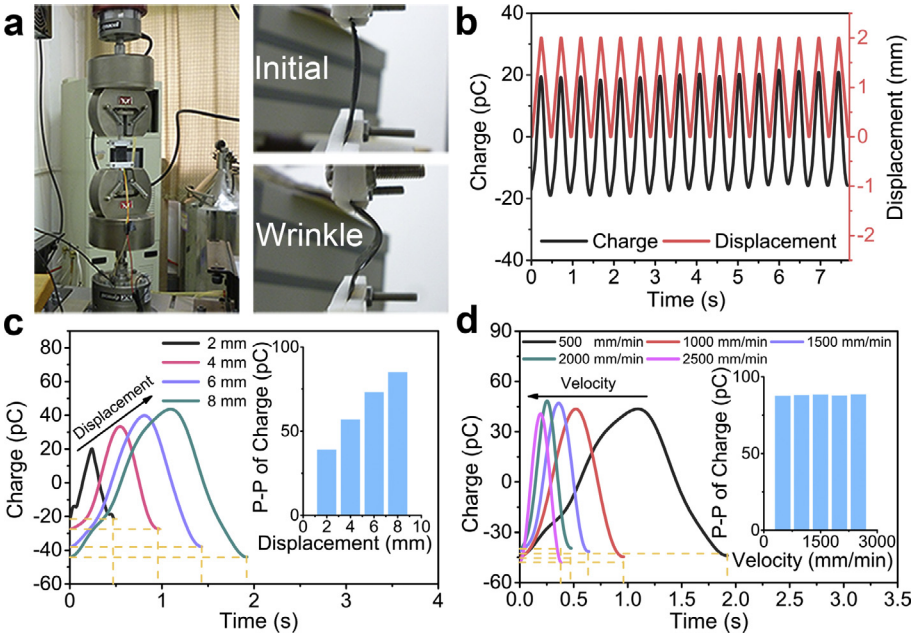

Fig. 6. (a) Experimental setup of cyclic wrinkle measurement of the actuator using instron. (b) Induced charge at the displacement of 2 mm and velocity of 500 mm/min. (c) Induced charge at a velocity of 500 mm/min and displacement varied from 2 mm to 8 mm. Inset: calculated peak-to-peak charge. (d) Induced charge at the displacement of 8 mm and velocity varied from 500 mm/min to 2500 mm/min. Inset: calculated peak-to-peak charge. (For interpretation of the references to color in this figure legend, the reader is referred to the web version of this article.)

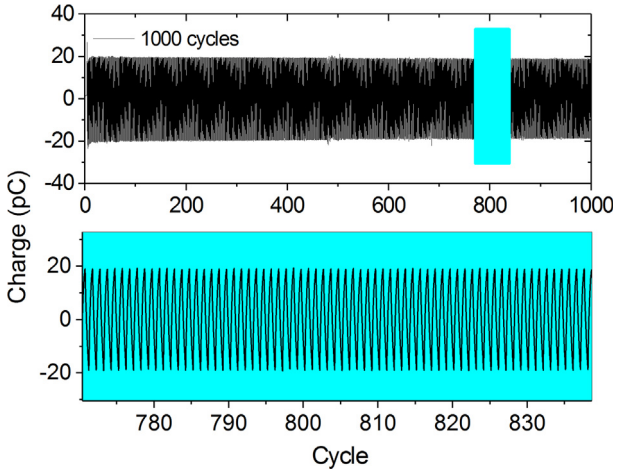

Fig. 7. The repeatability property of the actuator. (For interpretation of the references to color in this figure legend, the reader is referred to the web version of this article.)

tilever beam (Figs. 10a and S5). The deflection is very small and linear to the applied force (Fig.10b). Based on small strain assumption, the stiffness of cantilever beam can be calculated. Then, the magnetically induced force in magnetic stretching experiment can be obtained. The force, deflection and induced charge in magnetic stretching experiment are plotted in Fig.10c. These three parameters are positively correlated and increase with magnetic field. The magnetically induced force in the bending experiment is equal to that in stretching test due to the present of the same magnetic field. Finally, the magnetically induced force of bending experiment is calculated.

As discussed above, the pure bending effect can be calculated by subtracting the stretching effect from bending effect. The calculated results demonstrate that the induced charge of pure bending is almost kept as a constant at different magnetic fields (Fig.10d). For pure bending test, the average induced charge at different magnetic fields is 158 pC.

3.2.5. The theoretical analysis

In practical applications, the deformation of the actuator should be real-time measured in terms of intelligent control. Thus, it is necessary to investigate the relationship between induced charge and deformation to achieve real-time measurement. Previous works have studied the relationship between induced charge and deflection [31]. The existing models are almost based on small strain assumption and the formulas are always complex. Based on the previous works, we proposed a new model to study the deformation-dependent properties of the actuator (Fig.11a). The bending angle was chosen as a variable to replace the common deflection. The total induced charge Q is related to the electric polarization P as follows [31]:

$$Q = \int P dA \tag{1}$$

where A is the electrode area. The electric polarization P is given by [31]

$$P = \mu \frac{\partial \varepsilon_x}{\partial z} \tag{2}$$

In this equation, μ denotes the flexoelectric coefficient. ε_x is the strain along the length x direction and z is the direction along the depth of the actuator. Based on the thin plate theory [27], ε_x can be expressed as:

$$\varepsilon_x = z \frac{\partial^2 w(x)}{\partial x^2} \tag{3}$$

where $w(x)$ is the deflection of the actuator. For a small bending angle, the deflection $w(x)$ can be written as

$$w(x) = R - R\cos\theta \tag{4}$$

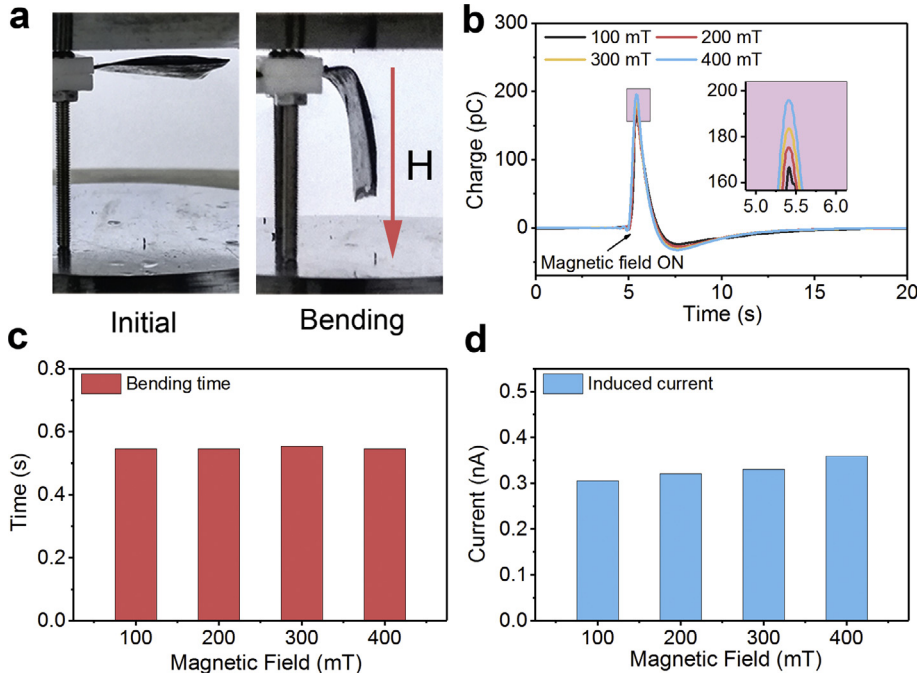

Fig. 8. (a) Photograph of the actuator at initial and bending state. (b) The induced charge curve in magnetic bending experiment. Inset: partially enlarged drawing of the peak charge. (c) The bending time of the actuator at different magnetic field. (d) The bending induced current of the actuator at different magnetic field. (For interpretation of the references to color in this figure legend, the reader is referred to the web version of this article.)

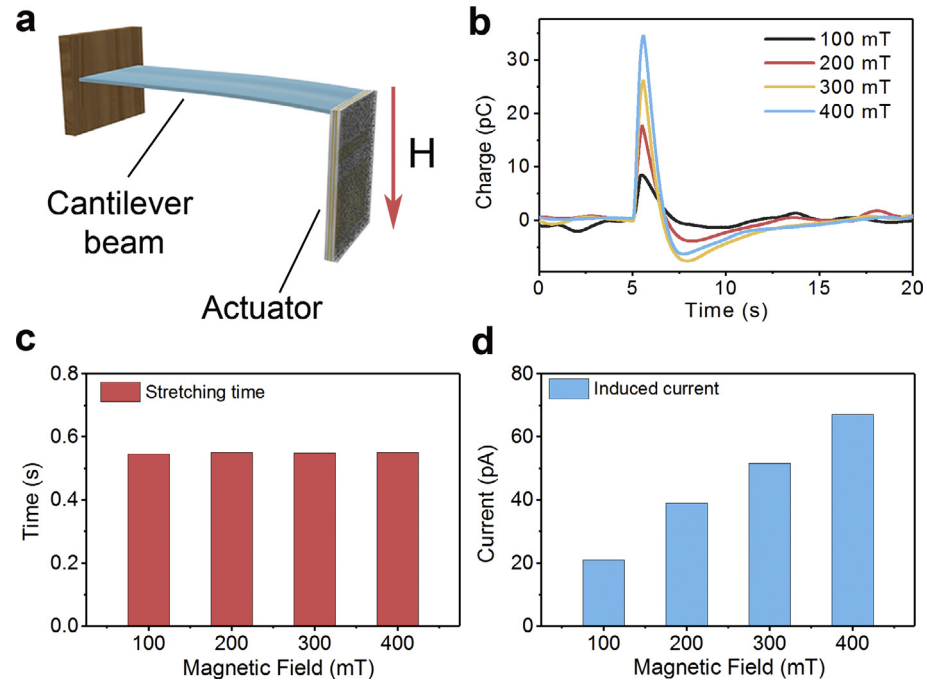

Fig. 9. (a) Schematic illustration of magnetic stretching experiment and (b) the corresponding results. (c) The stretching time of the actuator at different magnetic field. (d) The stretching induced current of the actuator at different magnetic field. (For interpretation of the references to color in this figure legend, the reader is referred to the web version of this article.)

where R is the radius of curvature of the bending deformation. θ is the bending angle corresponding to length x. Length x can be obtained by

$$x = R\sin\theta, \quad \theta \to 0 \tag{5}$$

By substituting (2), (3), (4), (5) in (1), we can derive

$$Q = \int PdA = \int_0^L Pbdx = \mu\frac{bL}{R} = \mu\frac{bR\theta}{R} = \mu b\theta \tag{6}$$

where b and L are the width and length of actuator respectively. As shown in Eq. (6), the induced charge Q is linear to the width b and bending angle θ. The flexoelectric coefficient μ is the inherent

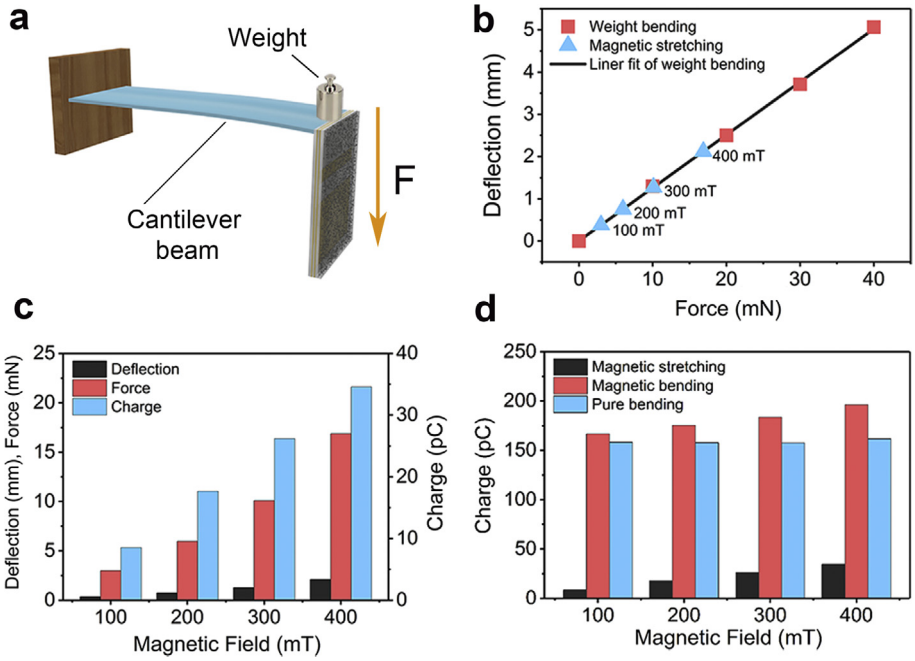

Fig. 10. (a) Schematic illustration of weight bending experiment. (b) The relationship between force and deflection. (c) Deflection, force, and induced charge of the actuator in magnetic stretching experiment. (d) The induced charge in magnetic stretching, magnetic bending and calculated pure bending experiment. (For interpretation of the references to color in this figure legend, the reader is referred to the web version of this article.)

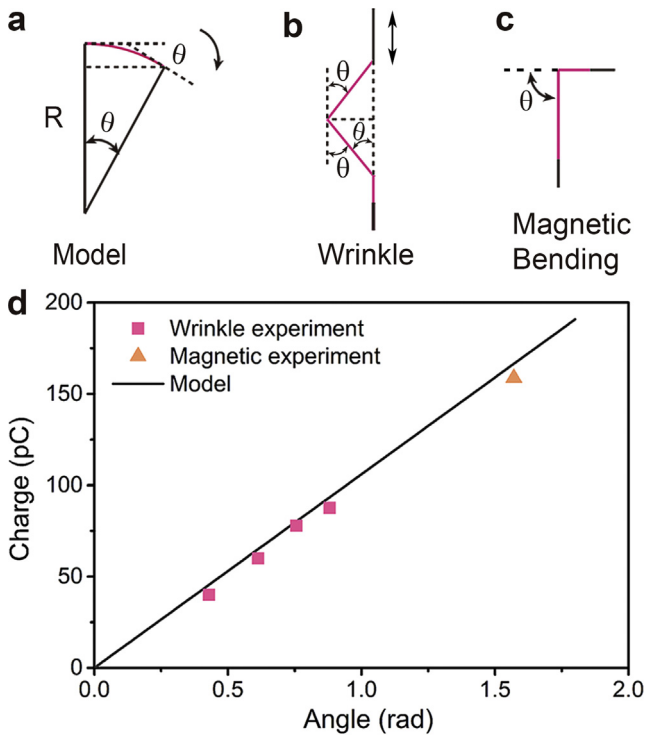

Fig. 11. (a) Schematic illustrations of proposed bending model. Schematic illustration of the bending angle in (b) wrinkle experiment and (c) magnetic bending experiment. (d) Comparison of the induced charge in wrinkle experiment, calculated pure magnetic bending experiment and modeling results. (For interpretation of the references to color in this figure legend, the reader is referred to the web version of this article.)

property of PVDF film. Meanwhile, the model is suitable for large range of bending deformation due to the absence of curvature R.

The wrinkle experiment can be simplified to the model in Fig.11b. The bending angle θ pointed out in the model can be written as

$$\theta = \cos^{-1}\left(\frac{(L-d)/2}{L/2}\right) = \cos^{-1}\left(\frac{L-d}{L}\right) \tag{7}$$

where d is the displacement in wrinkle experiment. According to the superposition property of charge, the final bending angle of wrinkle experiment is

$$\theta_{final} = 2\theta - \theta = \theta \tag{8}$$

The parameters for each displacement have been calculated according to the wrinkle experimental measurements. When the displacements are 2 mm, 4 mm, 6 mm, and 8 mm, the corresponding bending angles are 0.43 rad, 0.61 rad, 0.76 rad, and 0.88 rad, respectively. The magnetic bending experiment can be simplified to the model in Fig. 11c. The actual bending angle is nearly 1.57 rad for different magnetic field according to image processing.

The results of wrinkle experiment, calculated pure bending test, and model are illustrated in Fig. 11d. The measured charge indeed shows a nearly linear relationship with the bending angle. The slope of the curves is obtained from the bending angle-charge curve and the flexoelectric coefficient μ is calculated using Eq. (6). The value of flexoelectric coefficient μ is 6.32×10^{-9} C/m. Even though the experimental results are slightly smaller than the model due to the simplification of the actual conditions, the wrinkle and pure bending results fit the model very well. Therefore, the model is accurate and can be used in large range of deformation. Thus, this model is suitable for calculating the bending angle of actuator in complicated conditions.

Magnetically sensitive and flexible tentacle: grasping controllable and deformation real-time measurable

For artificial intelligent robotics, fast response is recommended for unpredictable conditions. Meanwhile, Real-time measurement is required to obtain the instantaneous status of the actuators, which is helpful to the information feedback and further active control. In this section, a magnetically sensitive and flexible

tentacle was manufactured by making full use of the existing actuator (Fig. 12a). The MAE film was cut into cross-shaped antenna (the size of each arm is 22 mm × 10 mm) with a copper stick fixed at the centre area. Then, four pieces of gold-plated PVDF films connected to conducting wires were separately packaged on the upper surface of antenna with PDMS. Thus, the compression happens only between MAE film and object. The conducting wire was connected to the upper surface of PVDF film. The length and width of the PVDF film are 22 mm and 5 mm. After that, the tentacle was obtained. The mass of the tentacle is 0.25 g. The tentacle was systematically studied with the custom control and measuring system (Fig. 12b). We firstly use a permanent magnet for demonstration (Fig. S6). In order to investigate the intelligent control property, an electromagnet was used to produce magnetic field. As demonstrated in Fig. 12c, the tentacle keeps unfolded initially on the top face of the ABS plastic. When turning on the current, the electromagnet can produce magnetic field and control the tentacle to grasp ABS plastic. The maximum magnetic field is only 100 mT. By keeping the current on and lifting the tentacle, the ABS plastic will be transported to the airspace above the electromagnet. The transportation distance of the tentacle was set as 10 mm. The real-time deformation of the tentacle was also measured when grasping and releasing the ABS plastic. As shown in Fig. 12d, the induced charge of the four arms increases rapidly when grasping the ABS plastic coincide with the deformation of tentacle arms. The time for deformation is as short as 0.5 s. The obtained negative charge is generated on the stretching side of bent PVDF film when grasping an object. The equivalent stretching induced charge can be calculated using equivalent model demonstrated in the Eq. (S1). Then, the pure bending induced charge of the tentacle can be obtained. Making full use of the proposed model, the bending angle of the arms of tentacle can be calculated (Fig. 12e). Although minor errors exist between the real bending angle and calculated bending angle, the calculated bending angle is consistent with the real one. Furthermore, the tentacle can grasp objects more than 3 times the weight of their own. Meanwhile, the energy density of the tentacle is estimated as $F_B\delta/2m$, where F_B is the force, δ is the displacement, and m is the mass of the tentacle [35]. The energy density of the tentacle when grasping ABS plastic is 0.15 J/kg.

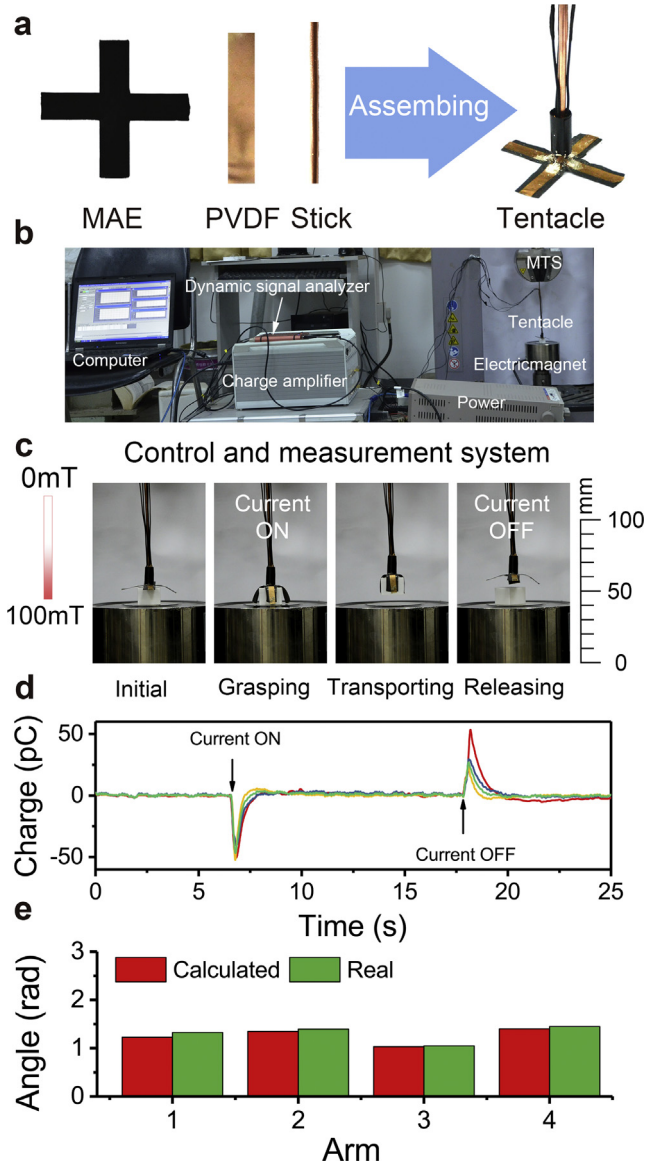

Fig. 12. (a) Photograph of cross-shaped MAE, PVDF, stick, and assembled tentacle. (b) Photograph of the custom control and measurement system. (c) Demonstration of the magnetic sensing tentacle used to grasp and release ABS plastic by switching the current. (d) Induced charge on four arms of tentacle when grasping and releasing the ABS plastic. (e) The calculated and real bending angle of tentacle when grasping ABS plastic. (For interpretation of the references to color in this figure legend, the reader is referred to the web version of this article.)

Thus, the tentacle can be used to grasp, transport, and release objects by switching the current. The deformation of the tentacle can be real-time measured with a quick feedback to control center for further active control. A computer controlled the whole process including current supply and real-time deformation measurement. This novel composite, which combines the outstanding properties of MAE film, such as magnetic sensitivity and controllability, with the flexoelectric advantages of PVDF, has wide application prospects in intelligent control devices.

4. Conclusions

In this work, a magnetically sensitive and controllable actuator consists of MAE and PVDF film was fabricated. The magnetic-mechanic-electric coupling properties of the actuator were systematically investigated. The actuator demonstrated high mechanic strength, good magnetic sensitivity, and excellent flexoelectricity. The induced charge shows excellent repeatability and increases with bending angle. The actuator exhibits excellent repeatability property. Magnetic bending and stretching tests were implemented to study the bending and stretching effect of the actuator at the present of magnetic field. The magnetically induced force, deflection, and charge were comprehensively studied. The pure bending effect was obtained by subtracting the stretching effect from bending effect. Based on the above experimental results, a linear dependence between induced charge and bending angle is demonstrated with a new proposed model. The model is in good agreement with the experimental results. Therefore, the novel model is accurate and can be used to measure the real-time deformation of the actuator. This new kind of artificial actuator has a quick response to magnetic field and can give feedback to the computer for further active control. Moreover, an actuator based magnetically sensitive tentacle was fabricated, which can be used to grasp, transport, and release objects in complex environments. Meanwhile, the deformation of the tentacle was real-time measured. The acquired information can be used to further control the external magnetic field. Therefore, this universal programming of tentacle preparation can enable engineers and scientists to design magnetically controllable and flexible actuators. This kind of actuators can find wide applications in engineering, artificial robotics, and biomedicine.

Acknowledgements

Financial support from the National Natural Science Foundation of China (Grant Nos. 11572310, 11572309), the Strategic Priority Research Program of the Chinese Academy of Sciences (Grant No. XDB22040502), and the Fundamental Research Funds for the Central Universities (WK2480000002) are gratefully acknowledged. This work is also supported by Collaborative Innovation Center of Suzhou Nano Science and Technology.

Appendix A. Supplementary material

Supplementary data associated with this article can be found, in the online version, at http://dx.doi.org/10.1016/j.compositesa.2017.09.004.

References

[1] Felton S, Tolley M, Demaine E, Rus D, Wood R. Applied origami. A method for building self-folding machines. Science 2014;345(6197):644–6.
[2] Xue Z, Tang Y, Duan X, Ye Y, Xie X, Zhou X. Ionic polymer–metal composite actuators obtained from sulfonated poly(ether ether sulfone) ion-exchange membranes. Compos Part A Appl Sci Manuf 2016;81:13–21.
[3] Huang HW, Sakar MS, Petruska AJ, Pane S, Nelson BJ. Soft micromachines with programmable motility and morphology. Nat Commun 2016;7:12263.
[4] Erb RM, Sander JS, Grisch R, Studart AR. Self-shaping composites with programmable bioinspired microstructures. Nat Commun 2013;4:1712.
[5] Ding L, Xuan S, Feng J, Gong X. Magnetic/conductive composite fibre: a multifunctional strain sensor with magnetically driven property. Compos Part A Appl Sci Manuf 2017;100:97–105.
[6] Li Y, Li J, Li W, Du H. A state-of-the-art review on magnetorheological elastomer devices. Smart Mater Struct 2014;23(12):123001.
[7] Fuhrer R, Schumacher CM, Zeltner M, Stark WJ. Soft iron/silicon composite tubes for magnetic peristaltic pumping: frequency-dependent pressure and volume flow. Adv Func Mater 2013;23(31):3845–9.
[8] Ausanio G, Iannotti V, Ricciardi E, Lanotte L, Lanotte L. Magneto-piezoresistance in magnetorheological elastomers for magnetic induction gradient or position sensors. Sens Actuators, A 2014;205:235–9.
[9] Lazarus N, Meyer CD, Bedair SS, Slipher GA, Kierzewski IM. Magnetic elastomers for stretchable inductors. ACS Appl Mater Interfaces 2015;7(19):10080–4.
[10] Olfatnia M, Cui L, Chopra P, Awtar S. Large range dual-axis micro-stage driven by electrostatic comb-drive actuators. J Micromech Microeng 2013;23(10):105008.
[11] Ye Z, Diller E, Sitti M. Micro-manipulation using rotational fluid flows induced by remote magnetic micro-manipulators. J Appl Phys 2012;112(6):064912.
[12] Tasoglu S, Diller E, Guven S, Sitti M, Demirci U. Untethered micro-robotic coding of three-dimensional material composition. Nat Commun 2014;5:3124.
[13] Fang FF, Liu YD, Choi HJ, Seo Y. Core-shell structured carbonyl iron microspheres prepared via dual-step functionality coatings and their magnetorheological response. ACS Appl Mater Interfaces 2011;3(9):3487–95.
[14] Kim YJ, Liu YD, Seo Y, Choi HJ. Pickering-emulsion-polymerized polystyrene/Fe_2O_3 composite particles and their magnetoresponsive characteristics. Langmuir 2013;29(16):4959–65.
[15] Pickering KL, Raa Khimi S, Ilanko S. The effect of silane coupling agent on iron sand for use in magnetorheological elastomers Part 1: Surface chemical modification and characterization. Compos Part A Appl Sci Manuf 2015;68:377–86.
[16] Stanier DC, Ciambella J, Rahatekar SS. Fabrication and characterisation of short fibre reinforced elastomer composites for bending and twisting magnetic actuation. Compos Part A Appl Sci Manuf 2016;91:168–76.
[17] Mishra SR, Dickey MD, Velev OD, Tracy JB. Selective and directional actuation of elastomer films using chained magnetic nanoparticles. Nanoscale 2016;8(3):1309–13.
[18] Choi S-B, Li W, Yu M, Du H, Fu J, Do PX. State of the art of control schemes for smart systems featuring magneto-rheological materials. Smart Mater Struct 2016;25(4):043001.
[19] Yang J, Du H, Li W, Li Y, Li J, Sun S, et al. Experimental study and modeling of a novel magnetorheological elastomer isolator. Smart Mater Struct 2013;22(11):117001.
[20] Volkova TI, Böhm V, Kaufhold T, Popp J, Becker F, Borin DY, et al. Motion behaviour of magneto-sensitive elastomers controlled by an external magnetic field for sensor applications. J Magn Magn Mater 2016;431:262–5.
[21] Marchi S, Casu A, Bertora F, Athanassiou A, Fragouli D. Highly magneto-responsive elastomeric films created by a two-step fabrication process. ACS Appl Mater Interfaces 2015;7(34):19112–8.
[22] Lum GZ, Ye Z, Dong X, Marvi H, Erin O, Hu W, et al. Shape-programmable magnetic soft matter. Proc Natl Acad Sci USA 2016;113(41):E6007–15.
[23] Lee S, Yim C, Kim W, Jeon S. Magnetorheological elastomer films with tunable wetting and adhesion properties. ACS Appl Mater Interfaces 2015;7(35):19853–6.
[24] Saleh Medina LM, Jorge GA, Rubi D, D'Accorso N, Negri RM. SBR/$BiFeO_3$ elastomer capacitor films prepared under magnetic and electric fields displaying magnetoelectric coupling. J Phys Chem C 2015;119(41):23319–28.
[25] Kim J, Chung SE, Choi SE, Lee H, Kim J, Kwon S. Programming magnetic anisotropy in polymeric microactuators. Nat Mater 2011;10(10):747–52.
[26] Gao W, Wang L, Wang X, Liu H. Magnetic driving flowerlike soft platform: biomimetic fabrication and external regulation. ACS Appl Mater Interfaces 2016;8(22):14182–9.
[27] Nguyen TD, Mao S, Yeh YW, Purohit PK, McAlpine MC. Nanoscale flexoelectricity. Adv Mater 2013;25(7):946–74.
[28] Wang B, Huang H-X. Incorporation of halloysite nanotubes into PVDF matrix: nucleation of electroactive phase accompany with significant reinforcement and dimensional stability improvement. Compos Part A Appl Sci Manuf 2014;66:16–24.
[29] Ahn Y, Lim JY, Hong SM, Lee J, Ha J, Choi HJ, et al. Enhanced piezoelectric properties of electrospun poly(vinylidene fluoride)/multiwalled carbon nanotube composites due to high β-phase formation in poly(vinylidene fluoride). J Phys Chem C 2013;117(22):11791–9.
[30] Poddar S, Ducharme S. Measurement of the flexoelectric response in ferroelectric and relaxor polymer thin films. Appl Phys Lett 2013;103(20):202901.
[31] Chu B, Salem DR. Flexoelectricity in several thermoplastic and thermosetting polymers. Appl Phys Lett 2012;101(10):103905.
[32] Lund A, Gustafsson C, Bertilsson H, Rychwalski RW. Enhancement of β phase crystals formation with the use of nanofillers in PVDF films and fibres. Compos Sci Technol 2011;71(2):222–9.
[33] Ghosh SK, Alam MM, Mandal D. The in situ formation of platinum nanoparticles and their catalytic role in electroactive phase formation in poly(vinylidene fluoride): a simple preparation of multifunctional poly(vinylidene fluoride) films doped with platinum nanoparticles. RSC Adv 2014;4(79):41886–94.
[34] Karan SK, Bera R, Paria S, Das AK, Maiti S, Maitra A, et al. An approach to design highly durable piezoelectric nanogenerator based on self-poled PVDF/AlO-rGO flexible nanocomposite with high power density and energy conversion efficiency. Adv Energy Mater 2016;6(20):1601016.
[35] Duduta M, Wood RJ, Clarke DR. Multilayer dielectric elastomers for fast, programmable actuation without prestretch. Adv Mater 2016;28(36):8058–63.